ADVANCED FUNCTIONAL MATERIALS

Supporting Information

for *Adv. Funct. Mater.,* DOI: 10.1002/adfm.202207136

2D Bismuthene as a Functional Interlayer between $BiVO_4$ and NiFeOOH for Enhanced Oxygen-Evolution Photoanodes

*Junyi Cui, Matyas Daboczi, Miriam Regue, Yi-Chun Chin, Katia Pagano, Jifang Zhang, Mark A. Isaacs, Gwilherm Kerherve, Aris Mornto, James West, Sixto Gimenez, Ji-Seon Kim, and Salvador Eslava**

Supporting Information

Two-Dimensional Bismuthene as a Functional Interlayer between $BiVO_4$ and NiFeOOH for Enhanced Oxygen-Evolution Photoanodes

*Junyi Cui, Matyas Daboczi, Miriam Regue, Yi-Chun Chin, Katia Pagano, Jifang Zhang, Mark A. Isaacs, Gwilherm Kerherve, Aris Mornto, James West, Sixto Gimenez, Ji-Seon Kim, and Salvador Eslava**

J. Cui, Dr. M. Daboczi, Dr. M. Regue, A. Mornto, J. West, and Dr. S. Eslava

Department of Chemical Engineering, Imperial College London, SW7 2AZ, London, United Kingdom

E-mail: s.eslava@imperial.ac.uk

Y. Chin, K. Pagano, and Prof. J. Kim

Department of Physics, Imperial College London, SW7 2AZ, London, United Kingdom

Dr. J. Zhang

School of Physical Science and Technology, ShanghaiTech University, Shanghai 201210, P. R. China

Prof. S. Gimenez

Institute of Advanced Materials (INAM), Universitat Jaume I, Castelló 12006, Spain

Dr. M. Isaacs

Department of Chemistry, University College London, London, WC1H 0AJ, United Kingdom

Dr. G. Kerherve

Department of Materials, Imperial College London, SW7 2AZ, London, United Kingdom

Keywords: 2D bismuthene, BiVO4 photoanodes, oxygen vacancies, co-catalysts, surface states

Experimental Methods

Synthesis of porous $BiVO_4$ photoanodes: $BiVO_4$ photoanodes were synthesized following a BiOI-assisted method[1] that we optimized for a superior reproducibility and performance. First, fluorine-doped tin oxide coated glass (Sigma-Aldrich) substrates were cleaned by ultrasonication in a 2% aqueous Hellmanex III solution, deionized water, acetone and isopropyl alcohol (each step for 3 min), followed by rinsing in deionized water. An ozone treatment of the FTO surface for 5 min to enhance its surface energy was also carried out. Secondly, a 50 mL aqueous plating solution was prepared containing 15 mM $Bi(NO_3)_3 \cdot 5H_2O$ (Sigma-Aldrich, 98%), 400 mM KI (Sigma-Aldrich, 99%) and 30 mM lactic acid (Sigma-Aldrich, 88-92%), with the pH adjusted to 1.8 using HNO_3 (Sigma-Aldrich, 70%). Thirdly, a 20 mL solution containing 46 mm p-benzoquinone (Sigma-Aldrich, 98%) in ethanol (VWR, ≥99.8%) was added slowly to the plating solution. The mixed solution was then stirred for 5 min and readjusted to a pH of 3.4 ± 0.05 using HNO_3 (Sigma-Aldrich, 70%). The resulting solution was used to electrodeposit a BiOI layer on the cleaned FTO-coated glass substrates. The electrodeposition was carried out at a potential of –0.35 $V_{Ag/AgCl}$ for 20 s, followed by a second step at a potential of –0.10 $V_{Ag/AgCl}$ for 17 min (0.37 C cm^{-2}). To transform the BiOI film into $BiVO_4$, it was first covered with 50 µL cm^{-2} of a 200 mM vanadyl acetylacetonate (Sigma-Aldrich, 98%) in dimethylsulfoxide (DMSO, Sigma-Aldrich, ≥99.9%), followed by a thermal treatment in air at 450 °C for 120 min (ramp rate 2 °C min^{-1}) in a tube furnace. Any excess of V_2O_5 was eliminated by immersing the film in a stirred aqueous solution of 1M NaOH (Sigma-Aldrich, ≥98%) for 30 min, followed by rinsing with deionized water and drying with a gentle air stream. The $BiVO_4$ photoanode preparation was concluded with an annealing in N_2 gas (research grade, BOC) at 350°C for 2 h (ramp rate 5°C min^{-1}) in a tube furnace. For this annealing, the $BiVO_4$ photoanode was mounted at an angle of 30° facing the N_2 flow.

Synthesis of bismuthene: 2D bismuthene was synthesized by reducing $BiCl_3$ with $NaBH_4$.[2] Firstly, a 50 mL solution of 1.5 mM $BiCl_3$ (Sigma-Aldrich, ≥98%) in 2-ethoxyethanol (Alfa Aesar, 99%) was prepared, and the mixture was ultrasonicated until a transparent solution was formed. The solution was then degassed of oxygen in a 120°C oil bath while continuously stirring under nitrogen gas bubbling. After cooling to ambient temperature, a 20 mL aqueous solution of 60 mM $NaBH_4$ (Sigma-Aldrich, ≥98%) was added dropwise for 5 minutes with

continuous stirring. A black precipitate was formed that was collected by centrifugation, washed twice with water and ethanol, dried at ambient temperature in a vacuum oven, and finally stored in a sealed container in an argon glovebox. Before use, large flakes were excluded by dispersing the bismuthene material in ethanol (0.1 mg ml^{-1}), followed by one first step of ultrasonication for 1 h and centrifugation at 1000 rpm for 10 min, and a second step of ultrasonication for 4 h and centrifugation at 3000 rpm for 5 min. TEM, atomic force microscopy (AFM) and dynamic light scattering (DLS) confirm the change in the flake size distribution from a few µm to ~50 nm upon these ultrasonication and centrifugation steps (**Figure S6**, Supporting Information).

Loading of bismuthene on $BiVO_4$: Bismuthene was loaded by immersing the photoanodes in a bismuthene suspension. Firstly, a $BiVO_4$ photoanode (3 x 2.5 cm^2) with the absorber side facing away from the beaker wall was immersed for 2 h in a 50 mL obtained ethanol suspension of ~50 nm bismuthene. Next, the photoelectrodes were dried at ambient temperature in a vacuum oven overnight. For consistency, bismuthene-free photoanodes were also immersed in a pure ethanol solution for the same duration.

*Electrodeposition of NiFeOOH:*NiFeOOH was loaded on $BiVO_4$ and $BiVO_4$/Bi photoanodes by photoelectrochemical deposition. Firstly, an activation step was implemented firstly to counter the hydrophobicity arising as an effect of the N_2 treatment. The electrode was submerged in a solution of 1 M borate buffer (sodium borate: Sigma-Aldrich, ≥99.5%, boric acid: Sigma-Aldrich, ≥99.5%) containing 0.2 M sodium sulfite (Sigma-Aldrich, ≥98%) kept at pH 9.3, and was subjected to potential sweeps between open-circuit potential and +0.45 $V_{Ag/AgCl}$, under one sun of illumination, repeating the sweep at least five times to get the sulfite oxidation current to converge. A careful rinsing with deionized water and drying with a gentle air stream followed. To load NiFeOOH, the $BiVO_4$ electrode was immersed in an aqueous solution of 40 mM $NiSO_4 \cdot 6H_2O$ (Sigma-Aldrich, ≥98%) and 10 mM $FeSO_4 \cdot 7H_2O$ (Sigma-Aldrich, ≥99%) was prepared using deionized water previously purged with N_2 gas for 30 min to eliminate any dissolved O_2. Then, then photoanode was immersed in this Ni^{2+}/Fe^{2+} aqueous solution for 5 min, and, afterwards, it was transferred into another aqueous solution containing 100 mM Na_2SO_4 (Sigma-Aldrich, ≥99%) at pH 8.0 ± 0.3, adjusted with NaOH. In this solution, the photoanode was irradiated with 3 mW cm^{-2} of simulated sunlight while connected to a Pt counter-electrode and a Ag/AgCl reference electrode, under an applied bias of +0.029 $V_{Ag/AgCl}$

for 70 s in the absence of stirring. This step was repeated from four to six times to pass a total of 4.2 mC cm^{-2}. Eventually, the photoanodes were careful rinsed with deionized water, dried with a gentle air stream, and stored in ambient air for a full day.

Characterization: X-ray diffraction (XRD) patterns were obtained using a Malvern Panalytical XRD X'Pert PRO system. UV-Vis diffuse reflectance spectra (DRS) were measured with a Shimadzu UV-3000 model equipped with an integrating sphere and $BaSO_4$ as white reference. Field emission gun scanning electron microscopy (SEM) micrographs were obtained using a LEO Gemini 1525 FEGSEM, at an electron high tension (EHT) of 5 kV. Transmission electron microscopy (TEM) and high-resolution TEM (HR-TEM) micrographs were obtained using a JEOL JEM-2100Plus electron microscope. Raman spectra were measured by using a Bruker Confocal Raman Microscope SENTERRA II. Atomic force microscopy (AFM) was performed on a Bruker AXS. Dynamic light scattering (DLS) of suspensions was obtained with a Malvern Panalytical Zetasizer μV. X-ray photoelectron spectroscopy (XPS) was carried out on a Thermo Fisher K-Alpha+ using monochromated Al Kα X-ray source. Binding energies were referenced relative to adventitious carbon at 284.6 eV. XPS data were processed using Avantage.

Cyclic voltammetry of bismuthene: Cyclic voltammetry (CV) was carried out on a rotating disk electrode (company name) with Pt as a counter-electrode and a Ag/AgCl reference electrode connected to a Ivium Compacstat potentiostat. First, a bismuthene ink was prepared by dispersing the filtered and washed bismuthene in a mixture of deionized water and ethanol (vol. 1:1) with a final concentration of 3 mg mL^{-1} of bismuthene. This suspension was ultrasonicated for 30 min for a better dispersion. After added Nafion solution (wt%=1:0.5), another 30 min of ultrasonication was employed. Next, 10 μL of this bismuthene ink was drop-casted on a glassy carbon disk of a rotating disk electrode and allowed to dry. CV curves were scanned in a potential range between –0.5 and +2 V_{RHE} in an 0.5 M Na_2SO_4 aqueous solution (pH 6) with a rotation speed of 1000 rpm.

PEC performance: Photoelectrochemical (PEC) measurements were carried out using a three-electrode setup, with photoanodes acting as the working electrode (active surface area 0.28

cm^2) against a Pt counter electrode and a KCl-saturated Ag/AgCl reference electrode (Alvatek, MF-2056). The electrolyte consisted of an aqueous 1 M potassium tetraborate buffer used to maintain the pH at 9. Sunlight was simulated with a Lot Quantum Design xenon lamp source equipped with an AM 1.5G filter and gauged with an International Light Technologies SEL033/U photodetector to 100 mW cm^{-2} at a controlled distance. The potential at the working electrode was controlled by using a Compactstat. potentiostat (Ivium Technologies). Scan rates were 10 mV s^{-1}. Reproducibility and error statistical analysis was carried out on more than three series of $BiVO_4$ photoanodes (see statistical analysis section).

Fermi level and SPV: A vibrating tip (gold alloy, 2 mm diameter) Kelvin probe (APS04, KP Technology) was applied to determine the potential difference between the sample and the tip. The tip work function (~4.6 eV) was calibrated by ambient photoemission spectroscopy using a cleaned silver reference. The work function was measured in dark, ambient condition for several hours and the saturated value was used to calculate the Fermi level. Surface photovoltage (SPV) signal was recorded by measuring the surface potential with the vibrating tip Kelvin probe first in dark, then for 150 s under white light illumination (20 mW cm^{-2}), and in dark for 100 s after turning the light off. In some cases, this cycle was repeated. Surface photovoltage spectroscopy was measured by the same setup but illuminating the sample with monochromatic light slowly scanning (90 s delay between steps) from 800 to 500 nm wavelength with 5 nm step size.

PEIS characterization: Photoelectrochemical impedance spectroscopy (PEIS) was conducted at various direct current (DC) potentials from +0.3 to +1.2 V_{RHE} at a step of 0.05 V and an alternating current (AC) potential of 10 mV with a frequency range of 100 kHz – 0. 1 Hz under simulated sunlight (Xe source, AM 1.5G filter, 100 mW cm^{-2}). All these measurements were carried out in a 1M KB buffer solution with pH 9 under simulated sunlight (Xe source, AM 1.5G filter, 100 mW cm^{-2}). Measurement with sacrificial agent was carried out by adding 100 mM $Fe(CN_6)^{3-/4-}$ to the same KB buffer solution. An equivalent circuit (EC) is used (**Figure 5a**, main manuscript**)**. Normally, a representative Nyquist plot for a $BiVO_4$ photoanode contains two semicircles that can be fitted using a two-RC-unit equivalent circuit.[3–6] However, depressed semicircles, instead of a perfect ones, are observed at low frequency. This is because, in the porous-structured $BiVO_4$, the time constant is no longer a constant, but a distribution.[7]

Hence, a constant phase element (CPE) is used to replace the interface capacitance. The capacitance of the CPE element is calculated using the following equation:[8]

$$C = \frac{1}{R}(RT)^{\frac{1}{P}} \qquad (1)$$

where *C* is the calculated capacitance, *R* is the resistance of the CPE. *T* is a magnitude with F s^n units, and *P* is a non-ideality factor with values between 0 (ideal resistance) and 1 (ideal capacitance), here fixed at P=0.7.

Since the high frequency semicircle is only related to the FTO layer, a simplified single RC equivalent circuit was used. The capacitances and resistances are extracted by fitting the low frequency semicircles.

IMPS characterization: Different from the PEIS which tabulates the applied bias, intensity-modulated photocurrent spectroscopy (IMPS) applies small perturbations of light at a fixed potential. The photogenerated charge carrier density is modulated sinusoidally by the time-dependent incident illumination. As a result, the relationship between the photocurrent response and light intensity, known as the transfer function (H), can be expressed in a complex plane. From this transfer function, we can assess surface kinetics of photoanodes. IMPS was conducted using a ModuLab XM PhotoEchem system (Solartron Analytical) with a 455 nm LED (Thorlab M455L3) illumination (37.5 mW cm^{-2}) at varying potentials from +0.3 to +1.3 V_{RHE} at a step of 0.05 V. A modulation of 10% in light intensity was applied, over a frequency range from 10^4 to 0.1 Hz at each potential step. The calculation of k_{rec}, k_{ct} and RC (τ) followed the method described by Prof. Laurence Peter:[3]

$$\omega_{max} = k_{ct} + k_{rec} \qquad (2)$$

$$\frac{LFI}{HFI} = \frac{k_{ct}}{(k_{ct} + k_{rec})} \qquad (3)$$

$$\tau = RC = 1/\omega_{min} \qquad (4)$$

where ω_{max} is the radial frequency at the maximum of the higher semicircle; ω_{min} is the radial frequency at the minimum of the lower semicircle; k_{ct} is the kinetics of charge transfer; k_{rec} is the kinetics of charge recombination; *LFI* is the intercept with x-axis at lower frequencies; *HFI* is the intercept with x-axis at higher frequencies; *RC* is the time constant of the system.

*Oxygen evolution detection:*Oxygen evolution on photoanodes was measured using a gastight PEC cell equipped with a TROXROB10 oxygen probe and a TDIP temperature sensor connected to a Pyroscience FireStingO_2 fiber-optic oxygen meter. The electrolyte was previously purged with N_2 for 30 min to remove any dissolved oxygen. The oxygen evolution was monitored every 20 s for 7200 s under simulated sunlight irradiation (Xe source, AM 1.5G filter, 100 mW cm^{-2}) at an applied bias of +0.8 V_{RHE}. The faradaic efficiency was calculated by dividing the measured amount of evolved O_2 by the theoretical amount of expected O_2 for the measured photocurrents (assuming 100% faradaic efficiency for oxygen evolution). The theoretical amount of O_2 was calculated by using the equation: $Q = n(e^-) \times F$, where *Q is* the charge (C); n(e^-) is the number of electrons (mol); and F is the Faraday constant (96485.3329 C mol^{-1}). 1 mol of O_2 is considered to involve 4 mol of e^-. The O_2 dissolved in the electrolyte solution was estimated using Henry's law and added to the values measured with the probe in the headspace.

IPCE test: The incident photon-to-current efficiency (IPCE) values of the photoanodes at different wavelengths (300–1000 nm) and a bias of +0.8 V_{RHE} and +1.23 V_{RHE} were determined using a 300 W Xe light source, an Acton Research monochromator (Spectra Pro 2155), and an electronic shutter (Uniblitz LS6). The intensity of monochromatic light was measured at the working electrode position with a SEL033/U 109 photodetector (International Light Technologies). The IPCE was calculated using the equation below:

$$IPCE = \frac{j_{ph}(mA\ cm^{-2}) \times 1239.8(V \times nm)}{P_{mono}(mW\ cm^{-2}) \times \lambda(nm)} \qquad (5)$$

where j_{ph} is the photocurrent density measured under single wavelength (λ) light illumination and P_{mono} is the incident irradiation power.

The integrated photocurrents were calculated from the product of the IPCE values and the photon intensity in the AM 1.5 G solar spectrum, downloaded from the National Renewable Energy Laboratory (NREL) website (global tilt, ASTM G173-03, www.nrel.gov/grid/solar-resource/spectra-am1.5.html, accessed on 1st Nov 2021).

Charge injection efficiency: The charge transfer efficiency at different applied bias was calculated using the following equation:

$$\eta_i = \frac{j_{PEC}\ (mA\ cm^{-2})}{j_{sac}(mA\ cm^{-2})} \times 100 \qquad (6)$$

where η_i is the charge injection efficiency, j_{PEC} is the photocurrent density measured in 1M KB buffer solution (pH 9) under simulated sunlight (Xe source, AM 1.5G filter, 100 mW cm^{-2}), and j_{sac} is the photocurrent measured in 1M KB buffer solution with 0.5 M Na_2SO_3 (pH 9) under the same simulated sunlight.

Statistical Analysis:

Pre-processing of data: All photocurrents and CV scans were normalized to mA cm^{-2} by dividing by the surface area of 0.28 cm^{-2} (PEC cell) or 0.19 cm^{-2} (RDE); The measured potentials vs. Ag/AgCl were converted to the reversible hydrogen electrode (RHE) scale according to the Nernst equation shown below:

$$E_{RHE} = E_{Ag/AgCl} + 0.059pH + E^0_{Ag/AgCl} \qquad (7)$$

Data is presented in the form of mean ± standard error. Sample size (n) for each statistical analysis was four. Excel sheets were used for statistical analysis.

Table S1. Summary of recently developed $BiVO_4$-based photoanodes

Photoanode	Co-catalyst	Photocurrent at +0.8 V_{RHE} (mA cm^{-2})	Photocurrent at +1.23 V_{RHE} (mA cm^{-2})	Ref.
$BiVO_4$	**Bismuthene/NiFeOOH**	**3.4(±0.2)**	**4.7(±0.2)**	**(This work)**
$BiVO_4$	BP/NiOOH	2.5	4.3	[9]
W:$BiVO_4$	amorphous Co-Pi	0.8	1.5	[10]
$BiVO_4$	$FeCoO_x$	2.5	4.8	[11]
$BiVO_4$	$La_{0.2}Co_{0.2}Ce_{0.6}O_x$	2	2.4	[12]
$BiVO_4$ with double amorphous TiO_2	Ir-COOH molecular catalysts	2.2	2.8	[13]
$BiVO_4$	cobalt salophen complexes	2.5	3.9	[14]
$BiVO_4$	TACo tannic acid coordinated with Co ions	2.5	4.8	[15]
$BiVO_4$	Rh 5%-doped $SrTiO_3$	0.5	0.8	[16]
$BiVO_4$/CdS heterojunction	NiCo-LDH	2.9	2.7	[17]
$BiVO_4$	$CuCoO_2$	2.2	3.3	[18]
$BiVO_4$	2D thin $Ti_3C_2T_X$ flakes	1.7	3.5	[19]
$BiVO_4$	Fe-Pi	1.8	2.3	[20]
Zr:$BiVO_4$	Ni-OH-Pi	1.7	3.2	[21]
V_2O_5@$BiVO_4$	amorphous NiOOH	0.5	1.2	[22]
$BiVO_4$	amorphous FeO_x	0.9	1.1	[23]
$BiVO_4$	CoMnZn LDH nanosheet	0.8	1.1	[24]
$BiVO_4$	FeOOH	1.5	2.1	[25]
$BiVO_4$	Fe_2TiO_5	1.5	3.2	[26]
$BiVO_4$	CoPi	0.8	1.1	[27]
Fe_2O_3/$BiVO_4$ heterojunction	NiFe-LDH nanosheets	0.8	1.7	[28]
$BiVO_4$	CoPi	1.5	2.2	[29]
W-doped $BiVO_4$	nickel-bicarbonate (Ni-Ci)	1.2	2.1	[30]
$BiVO_4$	NiO_x	1	0.5	[31]
$BiVO_4$	$Co_2N_{0.67}$ sheet	0.4	2.2	[32]
$BiVO_4$	ternary spinel $MnCo_2O_4$	2.4	2.8	[33]
Mo(0.3 at.%): $BiVO_4$	Ni/Sn	3.8	4.3	[34]
Pt:p-$BiVO_4$	N/A	4.3	5.4	[35]
Etched p-$BiVO_4$	CoPi	4.4	6.1	[36]
$BiVO_4$/SnOx	Co_4O_4/pGO	4.3	5.9	[37]
B-$BiVO_4$	NiFeV LDHs	3.4	4.6	[38]
$BiVO_4$	NiO/CoO_x	3.0	3.9	[39]
$BiVO_4$	$NiFeO_x$-B	4.1	4.9	[40]

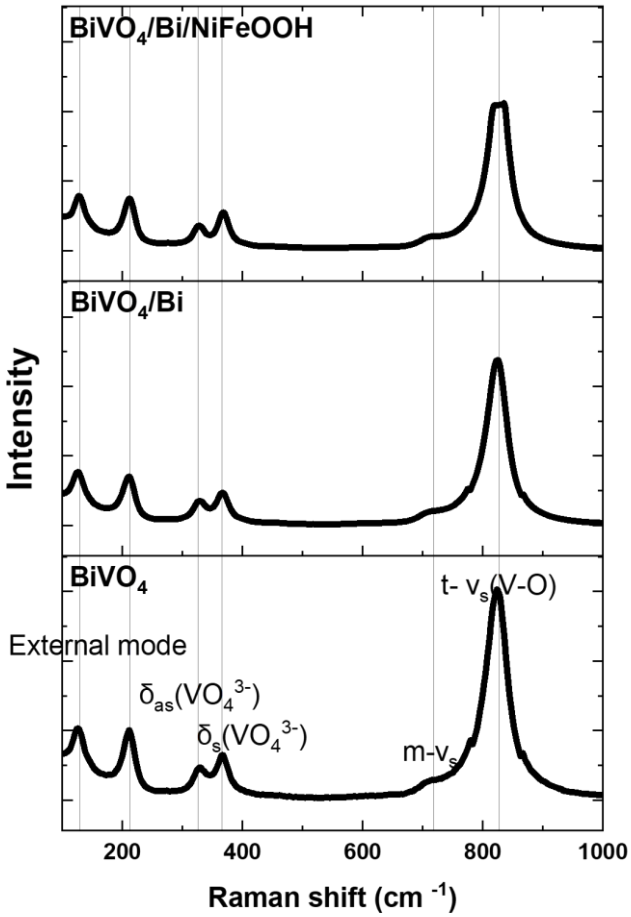

Figure S1. Raman spectra of photoanodes (from the bottom to the top): $BiVO_4$, $BiVO_4$/Bi, and $BiVO_4$/Bi/NiFeOOH.

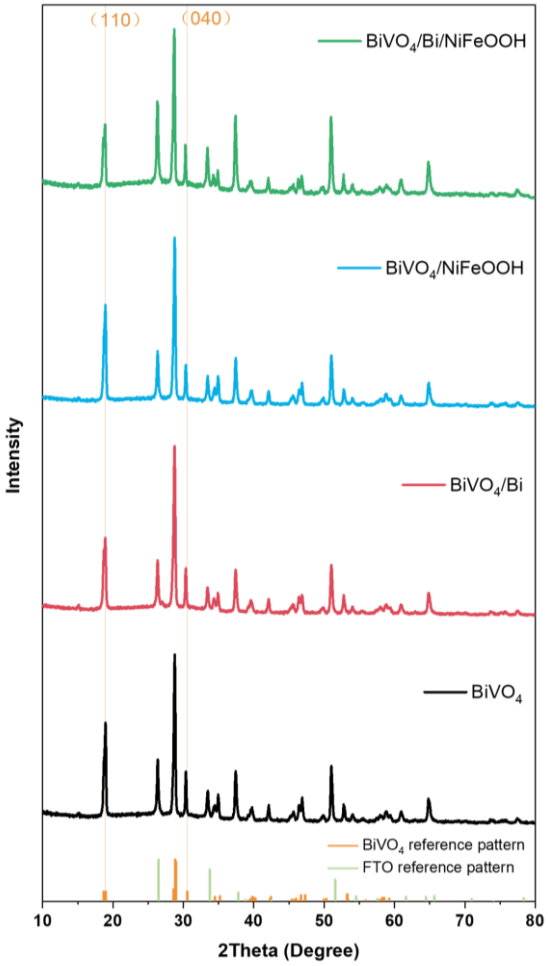

Figure S2. XRD patterns of photoanodes: $BiVO_4$ (black), $BiVO_4$/Bi (red), $BiVO_4$/NiFeOOH (blue), and $BiVO_4$/Bi/NiFeOOH (green). Reference patterns for $BiVO_4$ (number 00-014-0688) and FTO (number 00-041-1445) are included for comparison.

(a)

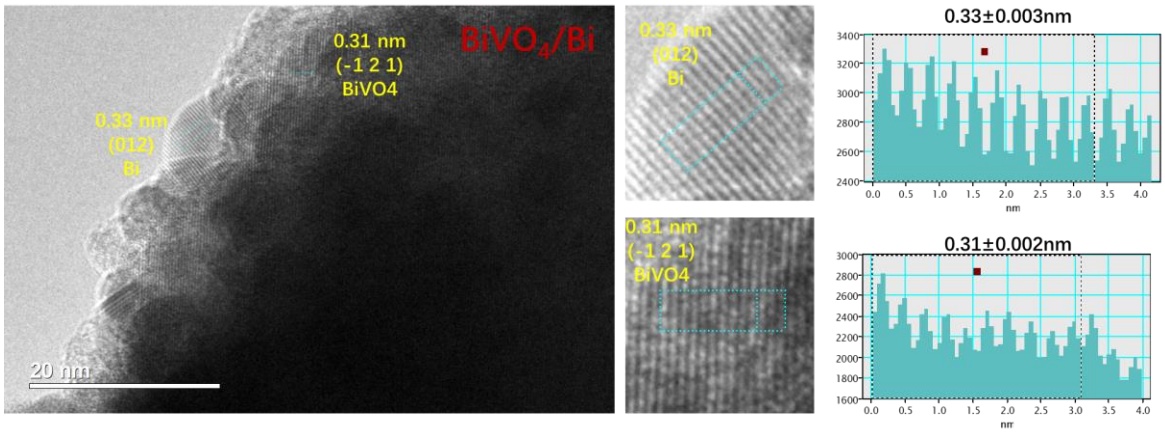

(b)

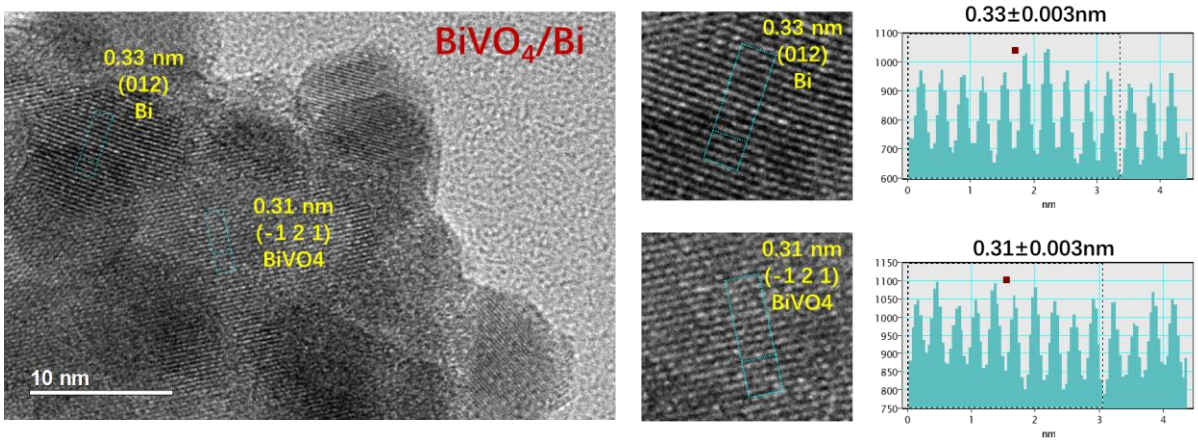

(c)

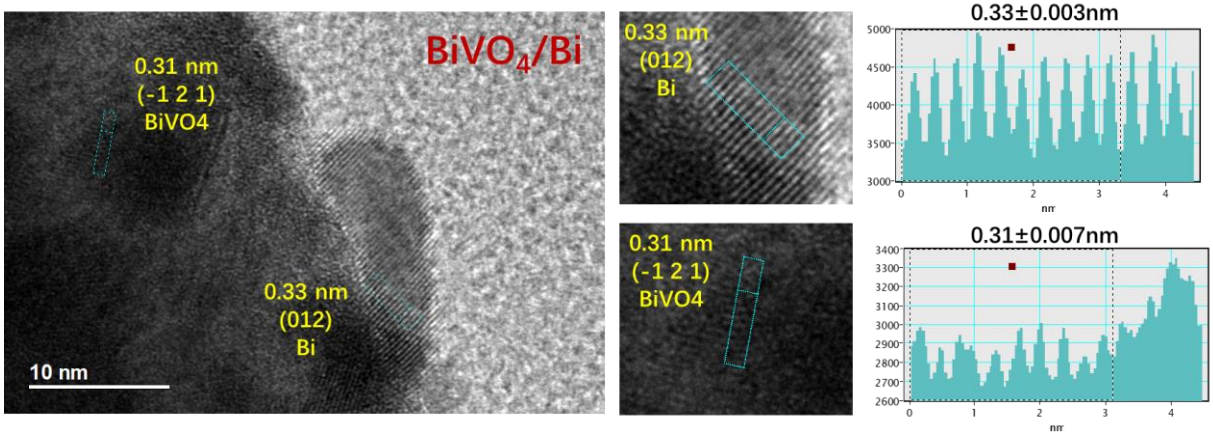

Figure S3 (a-c). HR-TEM micrographs of $BiVO_4$/Bi photoanodes and lattice space calculation ($BiVO_4$: JCPDS 00-014-0688; Bi: JCPDS 00-044-1246).

(d)

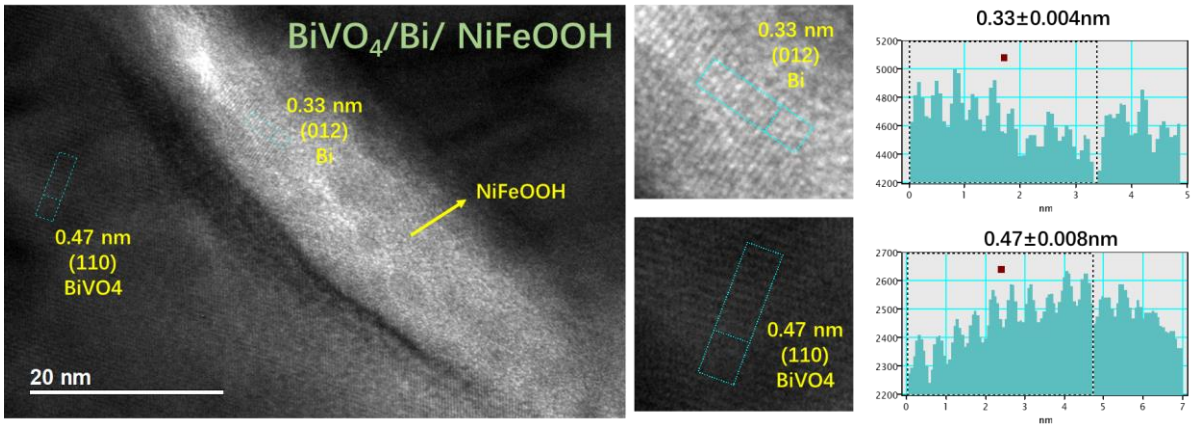

(e)

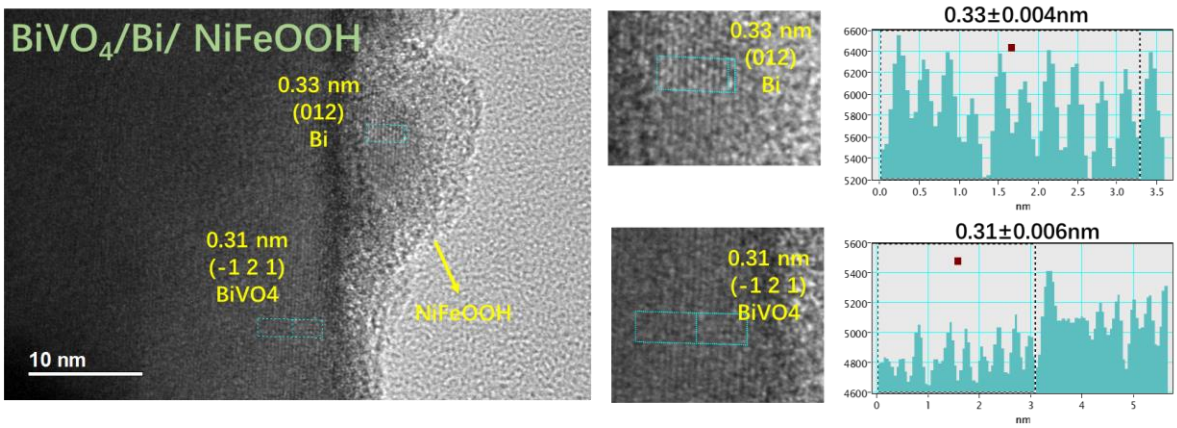

(f)

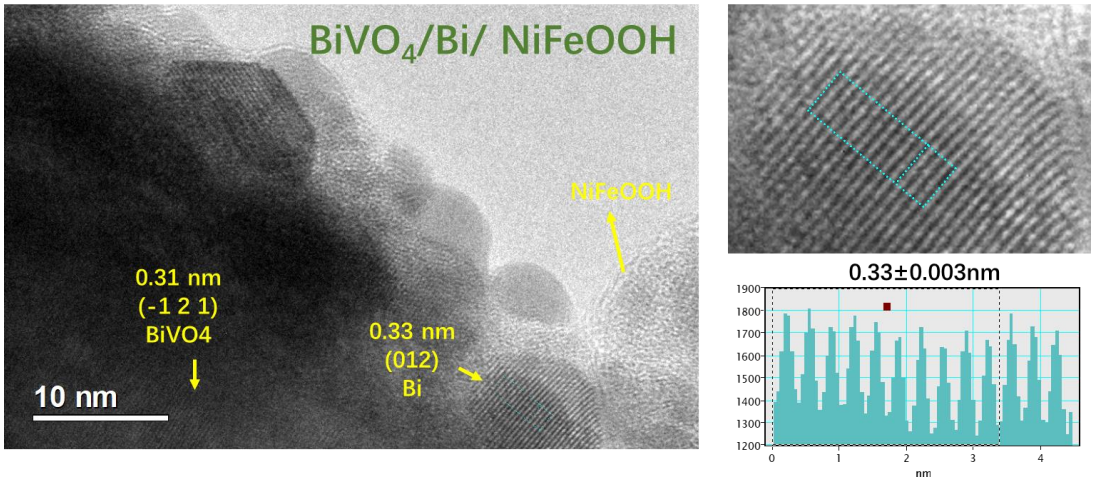

Figure S3 (d-f). HR-TEM micrographs of $BiVO_4$/Bi/NiFeOOH photoanodes and lattice space calculation ($BiVO_4$: JCPDS 00-014-0688; Bi: JCPDS 00-044-1246). (g)

Figure S3 (g). HR-TEM micrographs of $BiVO_4$/ NiFeOOH photoanodes.

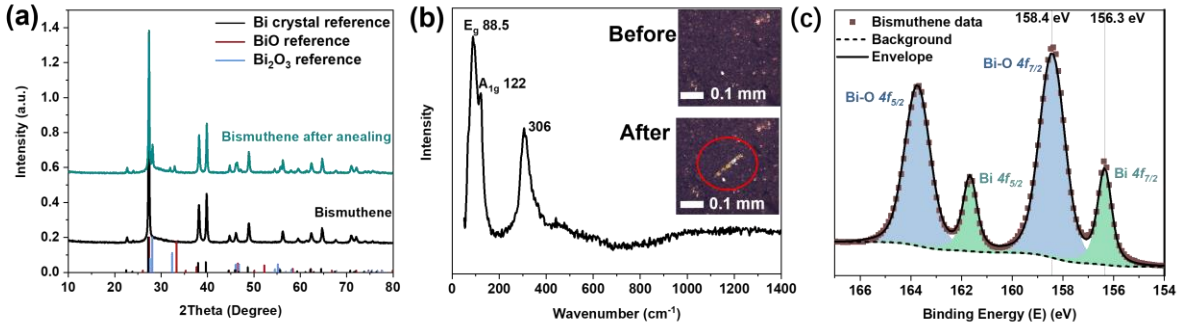

Figure S4. (a) XRD patterns of bismuthene before and after annealing at 200 °C in air for 1 h. (b) Raman spectrum of bismuthene measured in air (inset: optical micrographs before and after Raman test). (c) XPS Bi *4f* spectrum of bismuthene.

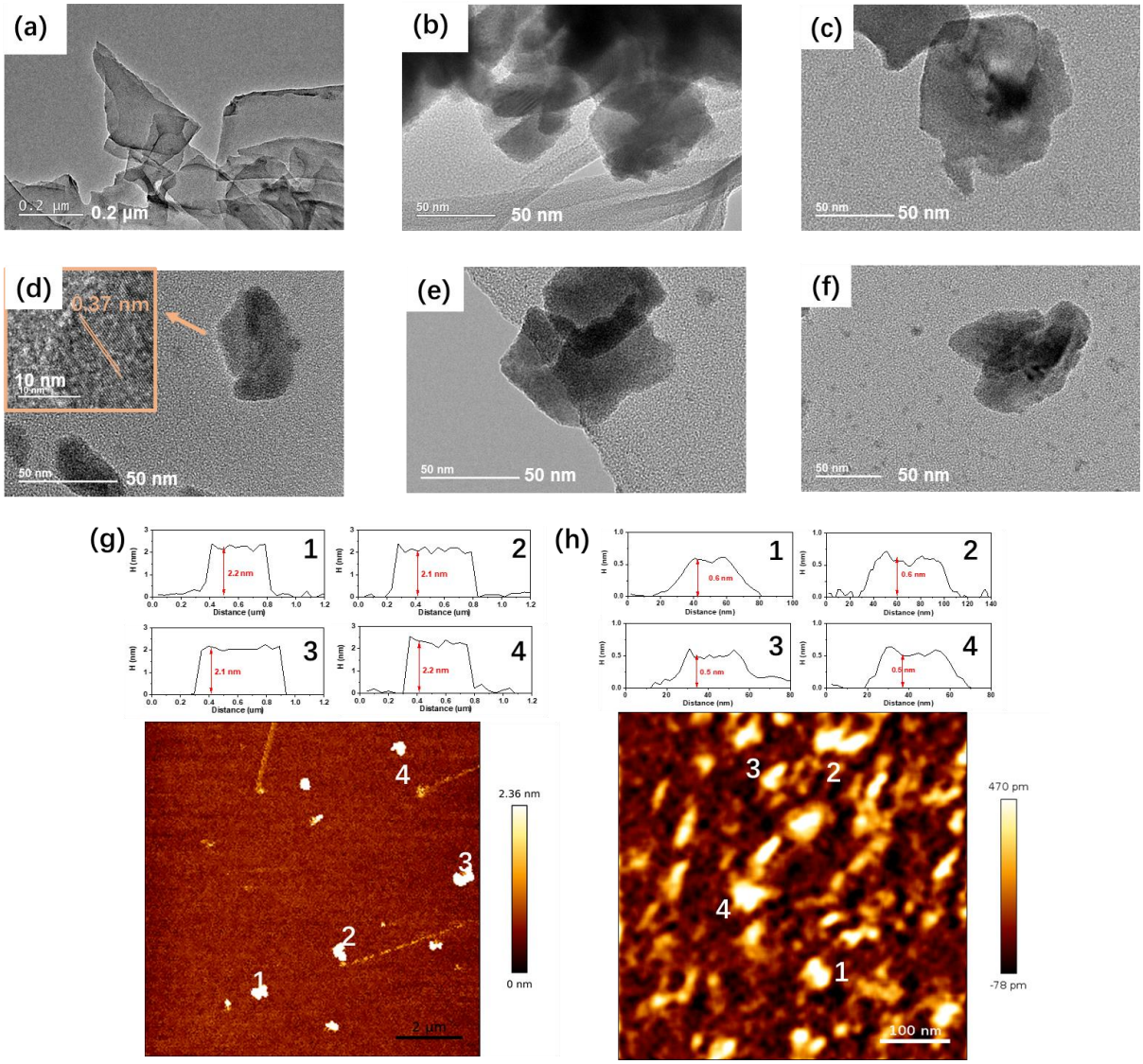

Figure S5. TEM micrographs of bismuthene (a) before and (b-f) after ultrasonication and centrifugation steps to decrease flake size. AFM micrographs of bismuthene (g) before and (h) after ultrasonication and centrifugation steps to decrease flake size.

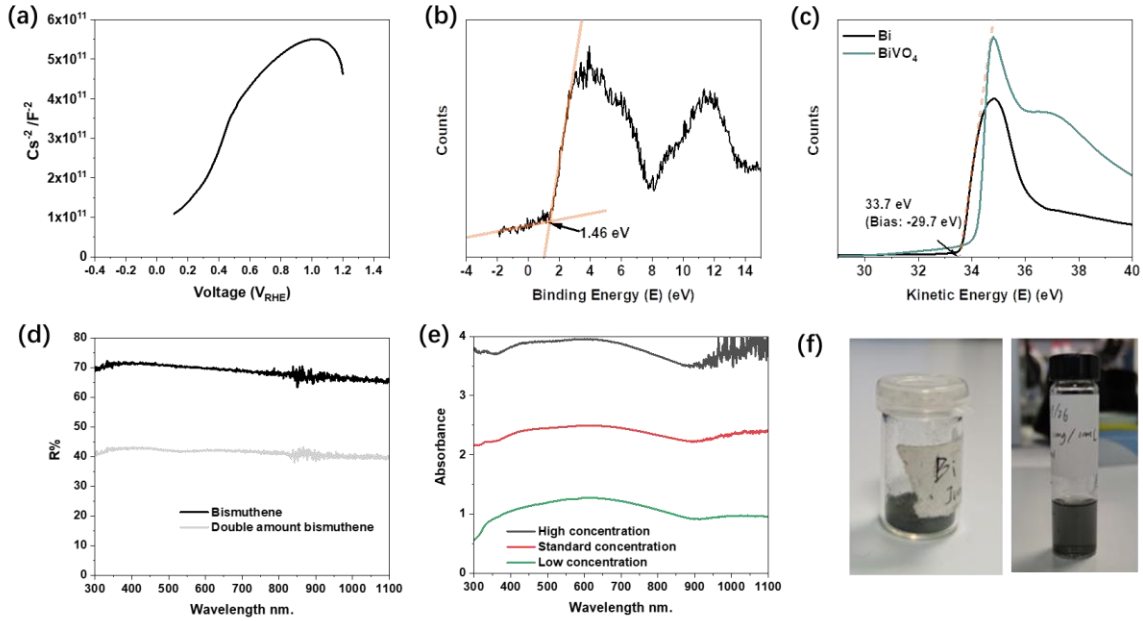

Figure S6: (a) Mott-Schottky plot of bismuthene deposited on a glassy carbon electrode measured in 1M KB buffer solution (pH 9); (b) valence band XPS spectrum of bismuthene; (c) XPS secondary electron cut-off for work function measurement on bismuthene and $BiVO_4$; (d) UV-Visible diffuse reflectance spectrum (UV-Vis DRS) of bismuthene powder with two different amounts on $BaSO_4$ white reference powder. (e) UV-Visible absorbance spectrum of bismuthene ethanol suspension with different concentrations. No clear absorption edge and/or band gap could be measured; (f) Photographs of bismuthene powder and ethanol suspension.

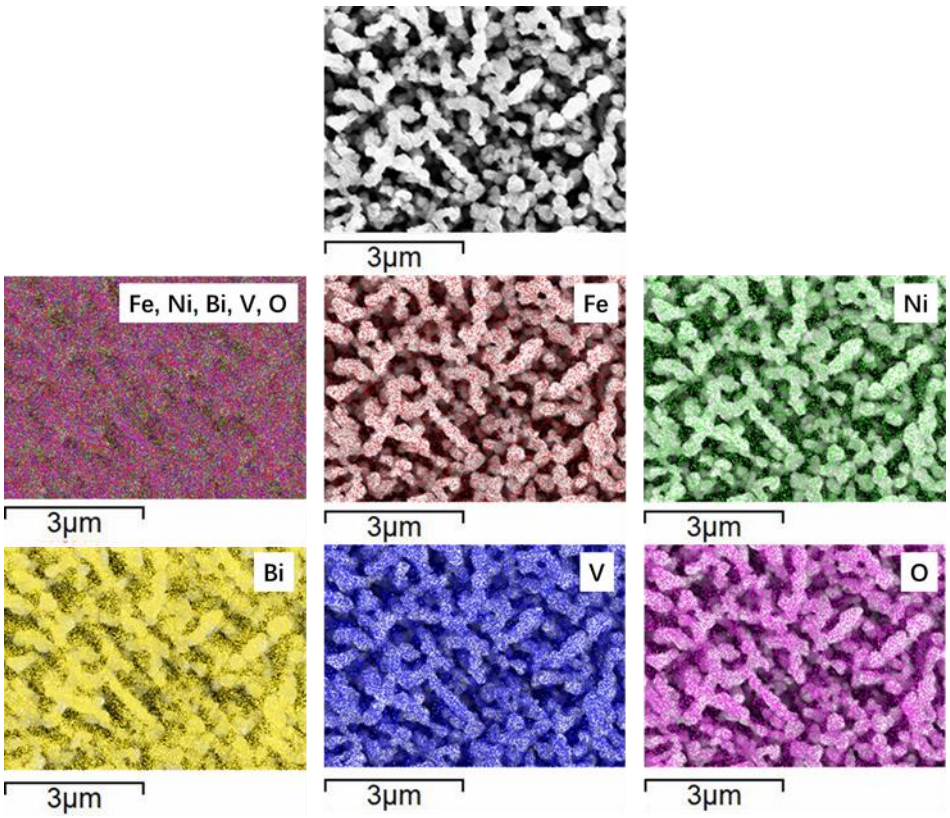

Figure S7. EDS mapping of a $BiVO_4$/Bi/NiFeOOH photoanode, including SEM micrograph, Fe element (red), Ni element (green), Bi element (yellow), V element (blue), and O element (purple).

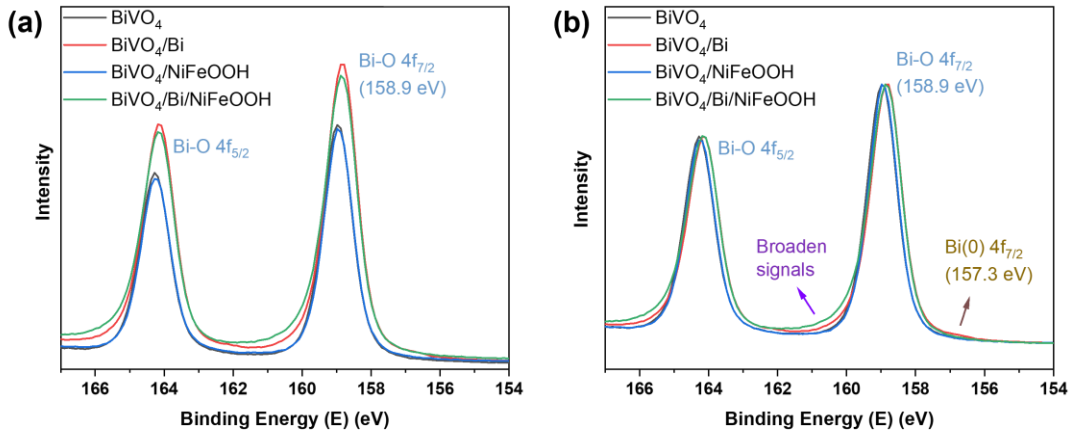

Figure S8. Bi *4f* XPS spectra of $BiVO_4$-based photoanodes: (a) Normalized by the areas of V $2p_{3/2}$ for showing the increase of Bi; (b) Normalized by the areas of Bi $4f_{7/2}$ for showing the broaden signals and Bi(0) peaks.

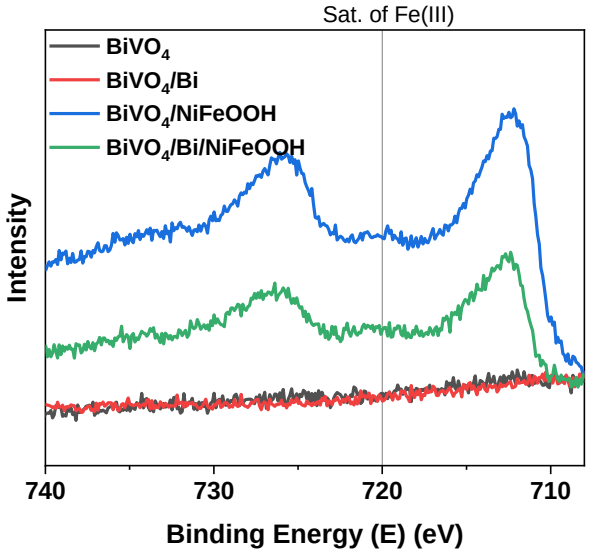

Figure S9. XPS Fe *2p* spectra of $BiVO_4$ photoanodes.

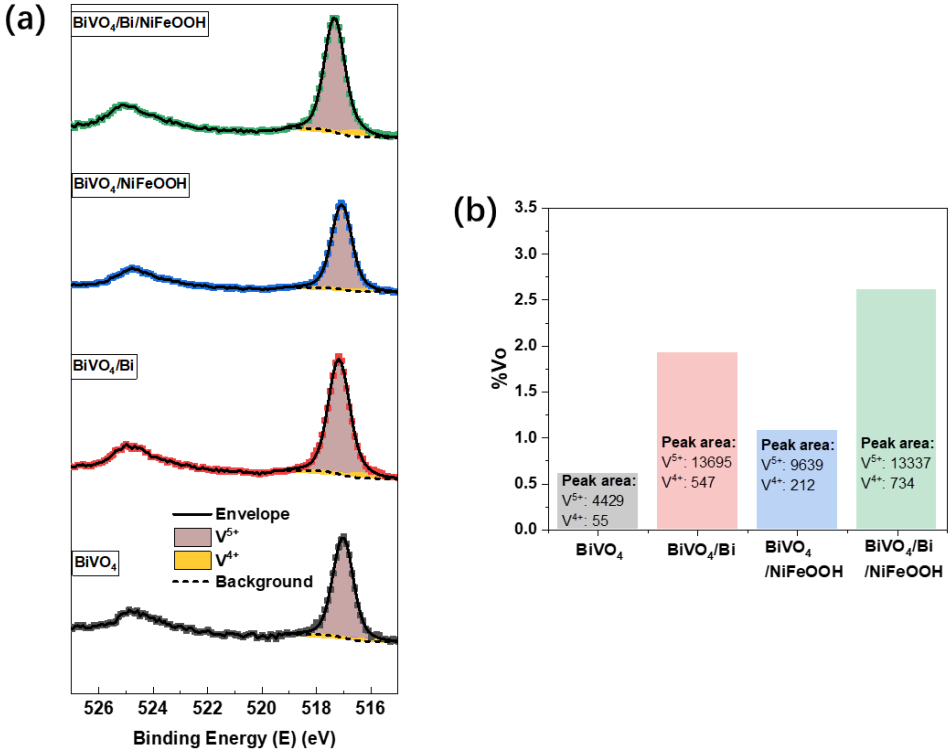

Figure S10. Repeated XPS spectra in a different series of samples to confirm XPS analysis reproducibility of Figure 2d: (a) XPS spectra of V *2p*. Scattered points correspond to raw data acquired in the measurements and solid lines to the fitted values. (b) Calculated atomic percentages of V_O from the relative area of V^{4+} and V^{5+}. Excess electrons from each oxygen vacancy site give rise to two equivalents of V^{4+}*species.*

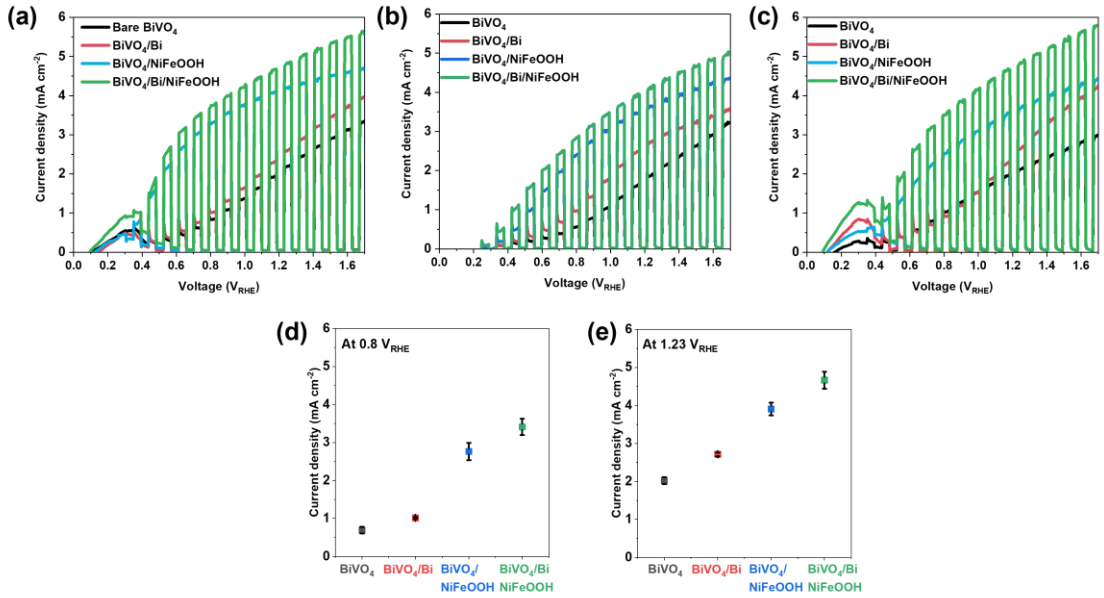

Figure S11. (a-c) Reproducibility and (d-e) error statistical analysis on photocurrent density-voltage curves of $BiVO_4$ photoanodes with chopped illumination. Voltage scan rate: 10 mV s^{-1}. Xe source, AM 1.5G filter, 100 mW cm^{-2}.

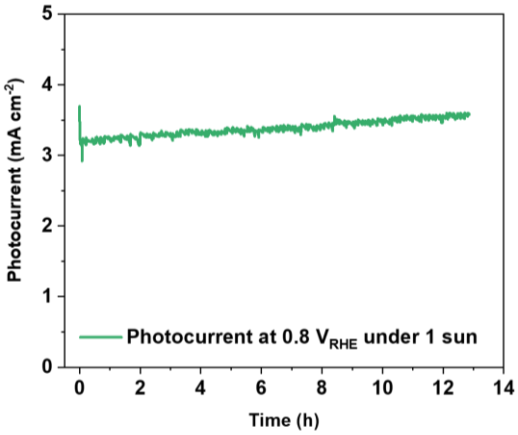

Figure S12. Photocurrent density stability tests of the $BiVO_4$/Bi/NiFeOOH photoanode in a 1M KB buffer solution with pH 9 under simulated sunlight (Xe source, AM 1.5G filter, 100 mW cm^{-2})

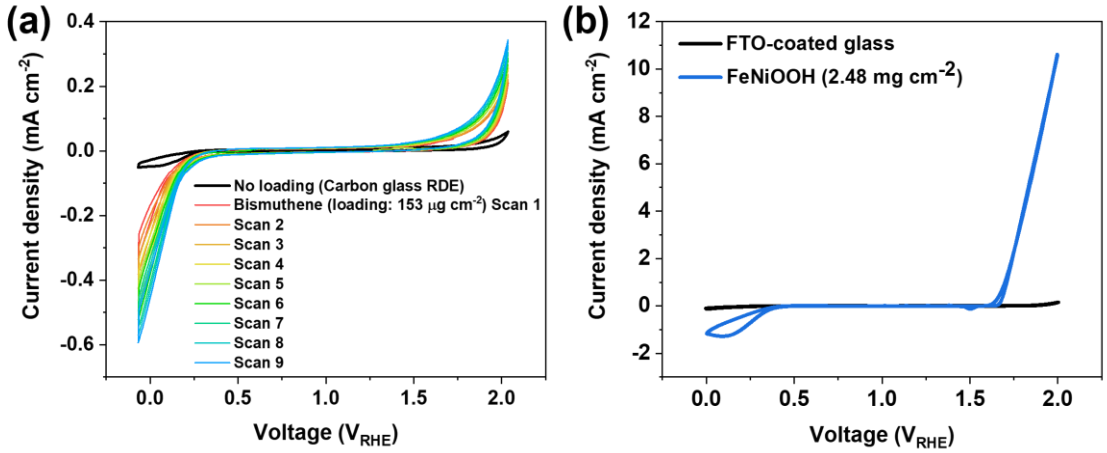

Figure S13. (a) CV curves in the dark: bismuthene loaded on RDE; (b) CV curves in the dark: NiFeOOH electrodeposited on FTO-coated glass.

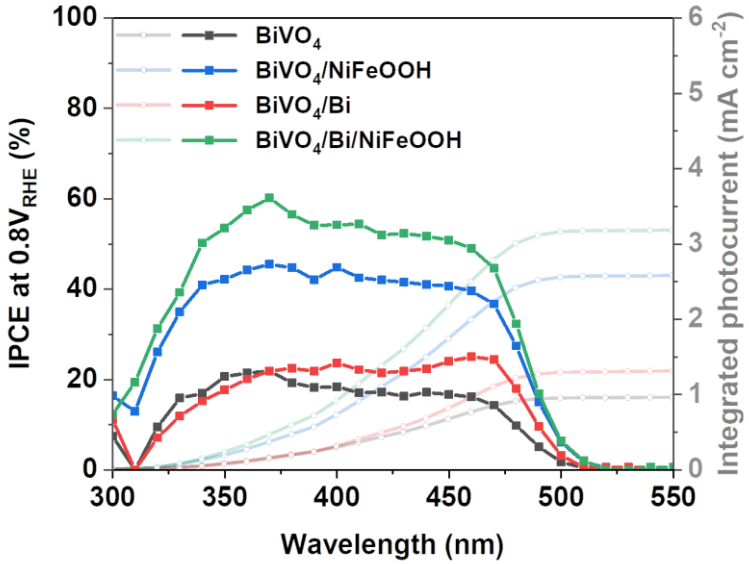

Figure S14. IPCE plots of $BiVO_4$ photoanodes at +0.8 V_{RHE} (left) and integrated photocurrents (right).

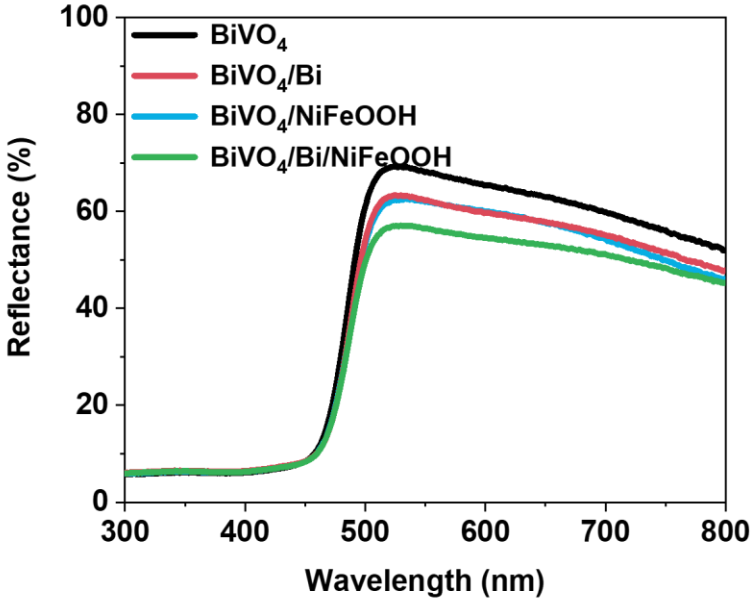

Figure S15. UV-Vis DRS spectra of $BiVO_4$ photoanodes.

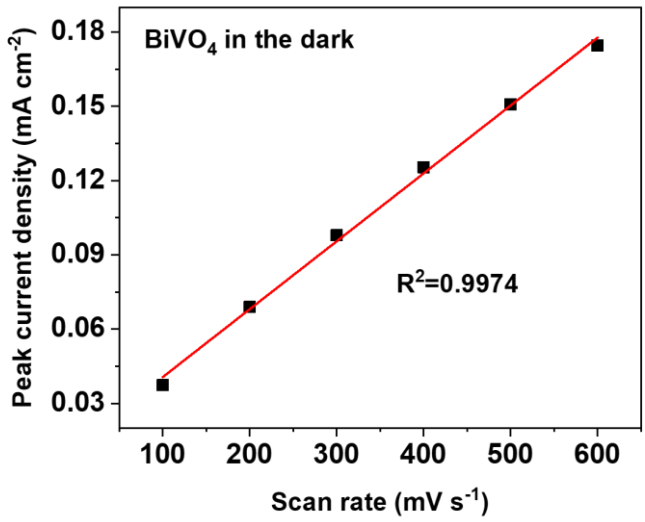

Figure S16. Linear relationship between peak current and scan rate obtained from CV of $BiVO_4$ at various scan rates in the dark

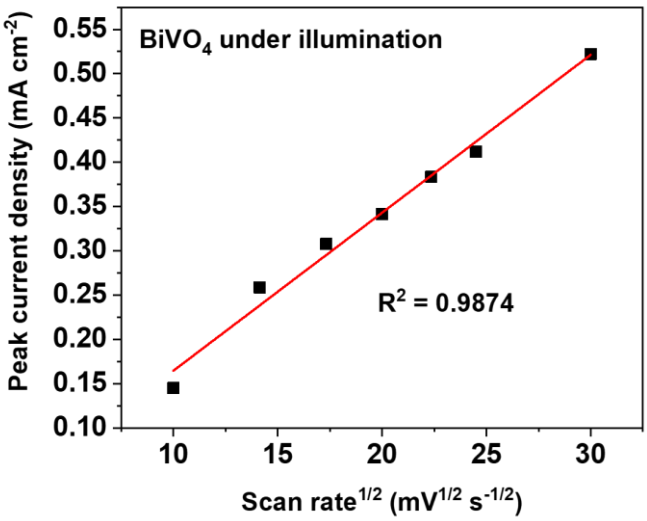

Figure S17. Linear relationship between peak current and $(\text{scan rate})^{1/2}$ obtained from CV of $BiVO_4$ at various scan rates under illumination.

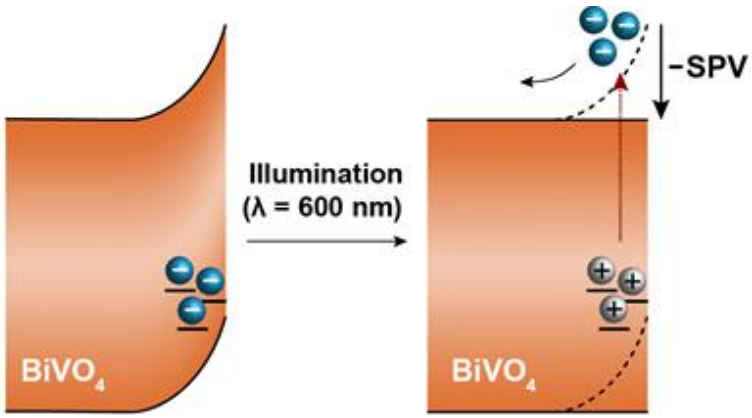

Figure S18. Schematic diagram of negative SPV signal generation after photoexcitation of electrons from trap states close to the valence band edge.

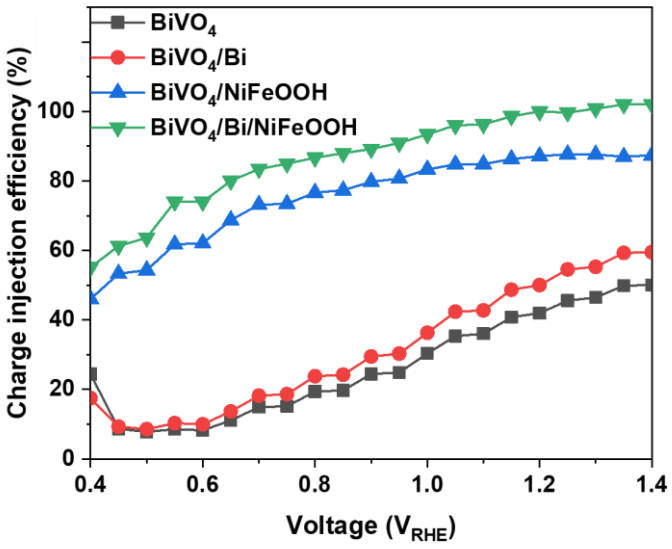

Figure S19. Charge injection efficiencies of photoanodes, calculated from the comparison of photocurrents with and without Na_2SO_3 hole scavenger in the electrolyte.

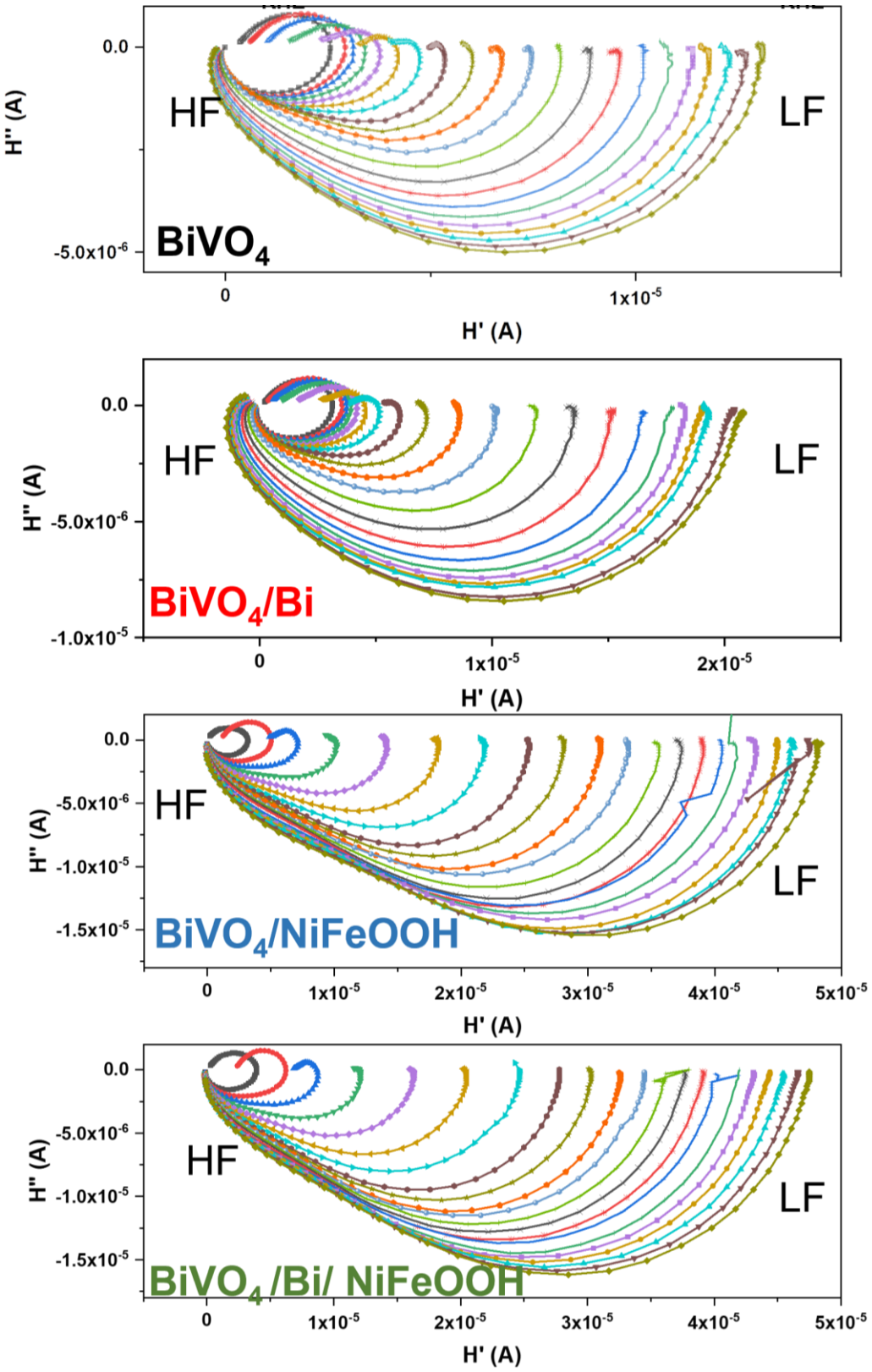

Figure S20. IMPS spectra of $BiVO_4$ photoanodes as a function of applied bias between +0.3 and +1.3 V_{RHE}.

Note 1:

$$W_{SC} = \left(\frac{2\varphi_{SC}\varepsilon\varepsilon_0}{qN}\right)^{1/2} \qquad (7)$$

where
W_{SC} is the width of the SCR
φ_{SC} is the potential drop across the SCR
ε is the relative permittivity of the semiconductor (68 for $BiVO_4$)
ε_0 is permittivity in vacuum (8.85×10^{-12} F m^{-1})
q is the charge of an electron (1.6×10^{-19} C)
N is the free carrier density (approx. 1×10^{24} m^{-3} for undoped $BiVO_4$)[41]

References

(1) Kim, T. W.; Choi, K. S. Nanoporous BiVO4 Photoanodes with Dual-Layer Oxygen Evolution Catalysts for Solar Water Splitting. *Science* **2014**, *343* (6174), 990–994. https://doi.org/10.1126/science.1246913.

(2) Yang, F.; Elnabawy, A. O.; Schimmenti, R.; Song, P.; Wang, J.; Peng, Z.; Yao, S.; Deng, R.; Song, S.; Lin, Y.; Mavrikakis, M.; Xu, W. Bismuthene for Highly Efficient Carbon Dioxide Electroreduction Reaction. *Nat. Commun.* **2020**, *11* (1), 1–8. https://doi.org/10.1038/s41467-020-14914-9.

(3) Parkinson, B.; Turner, J. *Photoelectrochemical Water Splitting: Materials, Processes and Architectures*; 2013. https://doi.org/10.1039/9781849737739-00001.

(4) Yu, F.; Li, F.; Yao, T.; Du, J.; Liang, Y.; Wang, Y.; Han, H.; Sun, L. Fabrication and Kinetic Study of a Ferrihydrite-Modified BiVO4 Photoanode. *ACS Catal.* **2017**, *7* (3), 1868–1874. https://doi.org/10.1021/ACSCATAL.6B03483.

(5) Shi, Q.; Murcia-López, S.; Tang, P.; Flox, C.; Morante, J. R.; Bian, Z.; Wang, H.; Andreu, T. Role of Tungsten Doping on the Surface States in BiVO4 Photoanodes for Water Oxidation: Tuning the Electron Trapping Process. *ACS Catal.* **2018**, *8* (4), 3331–3342. https://doi.org/10.1021/acscatal.7b04277.

(6) Li, T.; He, J.; Peña, B.; Berlinguette, C. P. Curing BiVO4 Photoanodes with Ultraviolet Light Enhances Photoelectrocatalysis. *Angew. Chemie Int. Ed.* **2016**, *55* (5), 1769–1772. https://doi.org/10.1002/ANIE.201509567.

(7) Hirschorn, B. D. *Distributed Time-Constant Impedance Responses Interpreted in Terms of Physically Meaningful Properties*; 2010.

(8) Mora-Seró, I.; Giménez, S.; Fabregat-Santiago, F.; Azaceta, E.; Tena-Zaera, R.; Bisquert, J. Modeling and Characterization of Extremely Thin Absorber (Eta) Solar Cells Based on ZnO Nanowires. *Phys. Chem. Chem. Phys.* **2011**, *13* (15), 7162–7169. https://doi.org/10.1039/C1CP20352E.

(9) Zhang, K.; Jin, B.; Park, C.; Cho, Y.; Song, X.; Shi, X.; Zhang, S.; Kim, W.; Zeng, H.; Park, J. H. Black Phosphorene as a Hole Extraction Layer Boosting Solar Water Splitting of Oxygen Evolution Catalysts. *Nat. Commun.* **2019**, *10* (1), 1–10. https://doi.org/10.1038/s41467-019-10034-1.

(10) Zhong, D. K.; Choi, S.; Gamelin, D. R. Near-Complete Suppression of Surface Recombination in Solar Photoelectrolysis by "Co-Pi" Catalyst-Modified W:BiVO4. *J. Am. Chem. Soc.* **2011**, *133* (45), 18370–18377. https://doi.org/10.1021/ja207348x.

(11) Wang, S.; He, T.; Yun, J. H.; Hu, Y.; Xiao, M.; Du, A.; Wang, L. New Iron-Cobalt Oxide Catalysts Promoting BiVO4 Films for Photoelectrochemical Water Splitting. *Adv. Funct. Mater.* **2018**, *28* (34), 1–10. https://doi.org/10.1002/adfm.201802685.
(12) Guevarra, D.; Shinde, A.; Suram, S. K.; Sharp, I. D.; Toma, F. M.; Haber, J. A.; Gregoire, J. M. Development of Solar Fuels Photoanodes through Combinatorial Integration of Ni-La-Co-Ce Oxide Catalysts on BiVO4. *Energy Environ. Sci.* **2016**, *9* (2), 565–580. https://doi.org/10.1039/c5ee03488d.
(13) Kan, M.; Xue, D.; Jia, A.; Qian, X.; Yue, D.; Jia, J.; Zhao, Y. A Highly Efficient Nanoporous BiVO4 Photoelectrode with Enhanced Interface Charge Transfer Co-Catalyzed by Molecular Catalyst. *Appl. Catal. B Environ.* **2018**, *225* (October 2017), 504–511. https://doi.org/10.1016/j.apcatb.2017.12.014.
(14) Liu, Y.; Jiang, Y.; Li, F.; Yu, F.; Jiang, W.; Xia, L. Molecular Cobalt Salophen Catalyst-Integrated BiVO 4 as Stable and Robust Photoanodes for Photoelectrochemical Water Splitting. *J. Mater. Chem. A* **2018**, *6* (23), 10761–10768. https://doi.org/10.1039/c8ta01304g.
(15) Tian, T.; Dong, C.; Liang, X.; Yue, M.; Ding, Y. Enhanced Photoelectrochemical Water Oxidation Activity of BiVO4 by Coating of Co-Phenolic Networks as Hole-Transfer and Co-Catalyst. *J. Catal.* **2019**, *377*, 684–691. https://doi.org/10.1016/j.jcat.2019.08.012.
(16) Zhang, Y.; Li, Y.; Ni, D.; Chen, Z.; Wang, X.; Bu, Y.; Ao, J. P. Improvement of BiVO4 Photoanode Performance During Water Photo-Oxidation Using Rh-Doped SrTiO3 Perovskite as a Co-Catalyst. *Adv. Funct. Mater.* **2019**, *1902101*, 1–10. https://doi.org/10.1002/adfm.201902101.
(17) Bai, S.; Li, Q.; Han, J.; Yang, X.; Shu, X.; Sun, J.; Sun, L.; Luo, R.; Li, D.; Chen, A. Photoanode of LDH Catalyst Decorated Semiconductor Heterojunction of BiVO4/CdS to Enhance PEC Water Splitting Efficiency. *Int. J. Hydrogen Energy* **2019**, *44* (45), 24642–24652. https://doi.org/10.1016/j.ijhydene.2019.07.214.
(18) Zhong, X.; He, H.; Du, J.; Ren, Q.; Huang, J.; Tang, Y.; Wang, J.; Yang, L.; Dong, F.; Bian, L.; Zhou, Y. Boosting Solar Water Oxidation Activity and Stability of BiVO 4 Photoanode through the Co-Catalytic Effect of CuCoO 2. *Electrochim. Acta* **2019**, *304*, 301–311. https://doi.org/10.1016/j.electacta.2019.02.101.
(19) Yan, D.; Fu, X.; Shang, Z.; Liu, J.; Luo, H. A BiVO 4 Film Photoanode with Re-Annealing Treatment and 2D Thin Ti 3 C 2 T X Flakes Decoration for Enhanced Photoelectrochemical Water Oxidation. *Chem. Eng. J.* **2019**, *361* (October 2018), 853–861. https://doi.org/10.1016/j.cej.2018.12.146.
(20) Vo, T. G.; Tai, Y.; Chiang, C. Y. Novel Hierarchical Ferric Phosphate/Bismuth Vanadate Nanocactus for Highly Efficient and Stable Solar Water Splitting. *Appl. Catal. B Environ.* **2019**, *243* (November 2018), 657–666. https://doi.org/10.1016/j.apcatb.2018.11.001.
(21) Shaddad, M. N.; Arunachalam, P.; Alothman, A. A.; Beagan, A. M.; Alshalwi, M. N.; Al-Mayouf, A. M. Synergetic Catalytic Behavior of AgNi-OH-Pi Nanostructures on Zr:BiVO 4 Photoanode for Improved Stability and Photoelectrochemical Water Splitting Performance. *J. Catal.* **2019**, *371*, 10–19. https://doi.org/10.1016/j.jcat.2019.01.024.
(22) Arunachalam, M.; Ahn, K. S.; Kang, S. H. Oxygen Evolution NiOOH Catalyst Assisted V 2 O 5 @BiVO 4 Inverse Opal Hetero-Structure for Solar Water Oxidation. *Int. J. Hydrogen Energy* **2019**, *44* (10), 4656–4663. https://doi.org/10.1016/j.ijhydene.2019.01.024.
(23) Saada, H.; Abdallah, R.; Fabre, B.; Floner, D.; Fryars, S.; Vacher, A.; Dorcet, V.; Meriadec, C.; Ababou-Girard, S.; Loget, G. Boosting the Performance of BiVO 4

Prepared through Alkaline Electrodeposition with an Amorphous Fe Co-Catalyst. *ChemElectroChem* **2019**, *6* (3), 613–617. https://doi.org/10.1002/celc.201801443.
(24) Vo, T. G.; Tai, Y.; Chiang, C. Y. Multifunctional Ternary Hydrotalcite-like Nanosheet Arrays as an Efficient Co-Catalyst for Vastly Improved Water Splitting Performance on Bismuth Vanadate Photoanode. *J. Catal.* **2019**, *370*, 1–10. https://doi.org/10.1016/j.jcat.2018.12.002.
(25) Chen, S. L.; Lin, L. Y.; Chen, Y. S. Improving the Photoelectrochemical Catalytic Ability of Bismuth Vanadate Electrodes by Depositing Efficient Co-Catalysts. *Electrochim. Acta* **2019**, *295*, 507–513. https://doi.org/10.1016/j.electacta.2018.10.174.
(26) Gao, Y.; Li, Y.; Yang, G.; Li, S.; Xiao, N.; Xu, B.; Liu, S.; Qiu, P.; Hao, S.; Ge, L. Fe2TiO5 as an Efficient Co-Catalyst to Improve the Photoelectrochemical Water Splitting Performance of BiVO4. *ACS Appl. Mater. Interfaces* **2018**, *10* (46), 39713–39722. https://doi.org/10.1021/acsami.8b14141.
(27) Nie, K.; Kashtanov, S.; Wei, Y.; Liu, Y. S.; Zhang, H.; Kapilashrami, M.; Ye, Y.; Glans, P. A.; Zhong, J.; Vayssieres, L.; Sun, X.; Guo, J. Atomic-Scale Understanding of the Electronic Structure-Crystal Facets Synergy of Nanopyramidal CoPi/BiVO4 Hybrid Photocatalyst for Efficient Solar Water Oxidation. *Nano Energy* **2018**, *53* (June), 483–491. https://doi.org/10.1016/j.nanoen.2018.09.001.
(28) Bai, S.; Chu, H.; Xiang, X.; Luo, R.; He, J.; Chen, A. Fabricating of Fe2O3/BiVO4 Heterojunction Based Photoanode Modified with NiFe-LDH Nanosheets for Efficient Solar Water Splitting. *Chem. Eng. J.* **2018**, *350* (May), 148–156. https://doi.org/10.1016/j.cej.2018.05.109.
(29) Ma, Y.; Kafizas, A.; Pendlebury, S. R.; Le Formal, F.; Durrant, J. R. Photoinduced Absorption Spectroscopy of CoPi on BiVO4: The Function of CoPi during Water Oxidation. *Adv. Funct. Mater.* **2016**, *26* (27), 4951–4960. https://doi.org/10.1002/adfm.201600711.
(30) Pilli, S. K.; Summers, K.; Chidambaram, D. Ni-Ci Oxygen Evolution Catalyst Integrated BiVO4 Photoanodes for Solar Induced Water Oxidation. *RSC Adv.* **2015**, *5* (58), 47080–47089. https://doi.org/10.1039/c5ra07262j.
(31) Liang, Y.; Messinger, J. Improving BiVO4 Photoanodes for Solar Water Splitting through Surface Passivation. *Phys. Chem. Chem. Phys.* **2014**, *16* (24), 12014–12020. https://doi.org/10.1039/c4cp00674g.
(32) Wan, X.; Su, J.; Guo, L. Enhanced Photoelectrochemical Water Oxidation on BiVO4 with Mesoporous Cobalt Nitride Sheets as Oxygen-Evolution Cocatalysts. *Eur. J. Inorg. Chem.* **2018**, *2018* (22), 2557–2563. https://doi.org/10.1002/ejic.201800392.
(33) Xu, D.; Xia, T.; Xu, H.; Fan, W.; Shi, W. Synthesis of Ternary Spinel MCo2O4 (M = Mn, Zn)/BiVO4 Photoelectrodes for Photolectrochemical Water Splitting. *Chem. Eng. J.* **2020**, *392* (March), 124838. https://doi.org/10.1016/j.cej.2020.124838.
(34) Kuang, Y.; Jia, Q.; Ma, G.; Hisatomi, T.; Minegishi, T.; Nishiyama, H.; Nakabayashi, M.; Shibata, N.; Yamada, T.; Kudo, A.; Domen, K. Ultrastable Low-Bias Water Splitting Photoanodes via Photocorrosion Inhibition and in Situ Catalyst Regeneration. *Nat. Energy 2016 21* **2016**, *2* (1), 1–9. https://doi.org/10.1038/nenergy.2016.191.
(35) Gao, R. T.; Liu, S.; Guo, X.; Zhang, R.; He, J.; Liu, X.; Nakajima, T.; Zhang, X.; Wang, L. Pt-Induced Defects Curing on BiVO4 Photoanodes for Near-Threshold Charge Separation. *Adv. Energy Mater.* **2021**, *11* (45), 2102384. https://doi.org/10.1002/AENM.202102384.
(36) Han, H. S.; Shin, S.; Kim, D. H.; Park, I. J.; Kim, J. S.; Huang, P. S.; Lee, J. K.; Cho, I. S.; Zheng, X. Boosting the Solar Water Oxidation Performance of a BiVO4 Photoanode by Crystallographic Orientation Control. *Energy Environ. Sci.* **2018**, *11* (5), 1299–1306. https://doi.org/10.1039/c8ee00125a.

(37) Ye, S.; Shi, W.; Liu, Y.; Li, D.; Yin, H.; Chi, H.; Luo, Y.; Ta, N.; Fan, F.; Wang, X.; Li, C. Unassisted Photoelectrochemical Cell with Multimediator Modulation for Solar Water Splitting Exceeding 4% Solar-to-Hydrogen Efficiency. *J. Am. Chem. Soc.* **2021**, *143* (32), 12499–12508. https://doi.org/10.1021/JACS.1C00802/SUPPL_FILE/JA1C00802_SI_001.PDF.

(38) Meng, Q.; Zhang, B.; Yang, H.; Liu, C.; Li, Y.; Kravchenko, A.; Sheng, X.; Fan, L.; Li, F.; Sun, L. Remarkable Synergy of Borate and Interfacial Hole Transporter on BiVO4photoanodes for Photoelectrochemical Water Oxidation. *Mater. Adv.* **2021**, *2* (13), 4323–4332. https://doi.org/10.1039/d1ma00344e.

(39) Zhong, M.; Hisatomi, T.; Minegishi, T.; Nishiyama, H.; Katayama, M.; Yamada, T.; Domen, K. Bulky Crystalline BiVO4 Thin Films for Efficient Solar Water Splitting. *J. Mater. Chem. A* **2016**, *4* (25), 9858–9864. https://doi.org/10.1039/c6ta03072f.

(40) Kuang, Y.; Jia, Q.; Nishiyama, H.; Yamada, T.; Kudo, A.; Domen, K. A Front-Illuminated Nanostructured Transparent BiVO4 Photoanode for >2% Efficient Water Splitting. *Adv. Energy Mater.* **2016**, *6* (2), 2–8. https://doi.org/10.1002/aenm.201501645.

(41) Ma, Y.; Pendlebury, S. R.; Reynal, A.; Formal, F. Le; Durrant, J. R. Dynamics of Photogenerated Holes in Undoped BiVO4 Photoanodes for Solar Water Oxidation. *Chem. Sci.* **2014**, *5* (8), 2964–2973. https://doi.org/10.1039/C4SC00469H.